HHS Public Access

Author manuscript

ACS Nano. Author manuscript; available in PMC 2024 April 20.

Published in final edited form as:

ACS Nano. 2024 April 16; 18(15): 10439–10453. doi:10.1021/acsnano.3c11374.

Self-Assembled STING-Activating Coordination Nanoparticles for Cancer Immunotherapy and Vaccine Applications

Xiaoqi Sun,
Department of Pharmaceutical Sciences, University of Michigan, Ann Arbor, Michigan 48109, United States; Biointerfaces Institute, University of Michigan, Ann Arbor, Michigan 48109, United States

Xuehui Huang,
Department of Pharmaceutical Sciences, University of Michigan, Ann Arbor, Michigan 48109, United States; Biointerfaces Institute, University of Michigan, Ann Arbor, Michigan 48109, United States

Kyung Soo Park,
Department of Biomedical Engineering and Biointerfaces Institute, University of Michigan, Ann Arbor, Michigan 48109, United States

Xingwu Zhou,
Department of Pharmaceutical Sciences, University of Michigan, Ann Arbor, Michigan 48109, United States; Biointerfaces Institute, University of Michigan, Ann Arbor, Michigan 48109, United States

Andrew A. Kennedy,
Department of Internal Medicine, University of Michigan Medical School, Ann Arbor, Michigan 48109, United States

Carla D. Pretto,

Corresponding Author: James J. Moon – Department of Pharmaceutical Sciences, University of Michigan, Ann Arbor, Michigan 48109, United States; Department of Biomedical Engineering, Biointerfaces Institute, Rogel Cancer Center, and Department of Chemical Engineering, University of Michigan, Ann Arbor, Michigan 48109, United States; moonjj@umich.edu.

Author Contributions

X.S., X.H., K.S.P., X.Z., and J.J.M. designed the experiments. X. S., X.H., K.S.P., and X.Z. performed the experiments. A.K., C.P., Q.W., Z.W., Y.X., and W.G. helped with specific experiments. X.S., X.H., K.S.P., X.Z., and J.J.M. analyzed and interpreted the data. X.S. and J.J.M. wrote the paper.

X.S., X.H., K.S.P., and X. Z. contributed equally to this work.

Complete contact information is available at: https://pubs.acs.org/10.1021/acsnano.3c11374

Supporting Information

The Supporting Information is available free of charge at https://pubs.acs.org/doi/10.1021/acsnano.3c11374.

Shown in Figures S1–S15 are photos of different coordination behaviors of CDA with various metal ions (Figure S1); EDAX mapping of the CDA–Zn–Mn crystal (Figure S2); serum cytokine level of mice after local injection of CDA or CDA–Zn–Mn (Figure S3); therapeutic effects of intratumoral CDA or CDA–Zn–Mn in subcutaneous B16F10 melanoma (Figure S4); EDAX mapping of ZMCP (Figure S5); characterization of ZMCP, ZCP, and MCP in PBS (Figure S6); drug retention in tumor after I.T. injection of ZMCP (Figure S7); tumor microenvironment modulation by ZMCP after intratumoral injection (Figure S8); therapeutic effects of intratumoral CDA–Zn–Mn and ZMCP (Figure S9); drug accumulation in tumor 24 h after I.V. injection of ZMCP (Figure S10); therapeutic effects of I.T. and I.V. injections of ZMCP therapy combined with immune checkpoint blockade against subcutaneous B16F10 melanoma (Figure S11); ZMCP-RBD induced effective T cell response against RBD sequences (Figure S12); retention and lymph node draining of ZMCP after subcutaneous injection (Figure S13); safety assessment of ZMCP after I.T. or I.V. injections (Figure S14); histological analysis of major organs after ZMCP-RBD and ZMCP-S1 vaccination (Figure S15) (PDF)

Department of Internal Medicine, University of Michigan Medical School, Ann Arbor, Michigan 48109, United States

Qi Wu,
Department of Pharmaceutical Sciences, University of Michigan, Ann Arbor, Michigan 48109, United States; Biointerfaces Institute, University of Michigan, Ann Arbor, Michigan 48109, United States

Ziye Wan,
Department of Pharmaceutical Sciences, University of Michigan, Ann Arbor, Michigan 48109, United States; Biointerfaces Institute, University of Michigan, Ann Arbor, Michigan 48109, United States

Yao Xu,
Department of Pharmaceutical Sciences, University of Michigan, Ann Arbor, Michigan 48109, United States; Biointerfaces Institute, University of Michigan, Ann Arbor, Michigan 48109, United States

Wang Gong,
Department of Periodontics and Oral Medicine, University of Michigan, Ann Arbor, Michigan 48109, United States; Department of Cancer Biology at the University of Texas M.D. Anderson Cancer Center, Houston, Texas 77030, United States

Jonathan Z. Sexton,
Department of Internal Medicine, University of Michigan Medical School, Ann Arbor, Michigan 48109, United States; Department of Medicinal Chemistry, College of Pharmacy, University of Michigan, Ann Arbor, Michigan 48109, United States

Andrew W. Tai,
Department of Internal Medicine and Department of Microbiology and Immunology, University of Michigan Medical School, Ann Arbor, Michigan 48109, United States

Yu Leo Lei,
Department of Periodontics and Oral Medicine, Department of Otolaryngology—Head and Neck Surgery, and Rogel Cancer Center, University of Michigan, Ann Arbor, Michigan 48109, United States; Department of Head and Neck Surgery, Department of Cancer Biology, Department of Translational Pathology, The University of Texas M.D. Anderson Cancer Center, Houston, Texas 77030, United States

James J. Moon
Department of Pharmaceutical Sciences, University of Michigan, Ann Arbor, Michigan 48109, United States; Department of Biomedical Engineering, Biointerfaces Institute, Rogel Cancer Center, and Department of Chemical Engineering, University of Michigan, Ann Arbor, Michigan 48109, United States

Abstract

The cGAS-STING pathway plays a crucial role in innate immune activation against cancer and infections, and STING agonists based on cyclic dinucleotides (CDN) have garnered attention for their potential use in cancer immunotherapy and vaccines. However, the limited drug-like

properties of CDN necessitate an efficient delivery system to the immune system. To address these challenges, we developed an immunostimulatory delivery system for STING agonists. Here, we have examined aqueous coordination interactions between CDN and metal ions and report that CDN mixed with Zn^{2+} and Mn^{2+} formed distinctive crystal structures. Further pharmaceutical engineering led to the development of a functional coordination nanoparticle, termed the Zinc–Mn–CDN Particle (ZMCP), produced by a simple aqueous one-pot synthesis. Local or systemic administration of ZMCP exerted robust antitumor efficacy in mice. Importantly, recombinant protein antigens from SARS-CoV-2 can be simply loaded during the aqueous one-pot synthesis. The resulting ZMCP antigens elicited strong cellular and humoral immune responses that neutralized SARS-CoV-2, highlighting ZMCP as a self-adjuvant vaccine platform against COVID-19 and other infectious pathogens. Overall, this work establishes a paradigm for developing translational coordination nanomedicine based on drug–metal ion coordination and broadens the applicability of coordination medicine for the delivery of proteins and other biologics.

Graphical Abstract

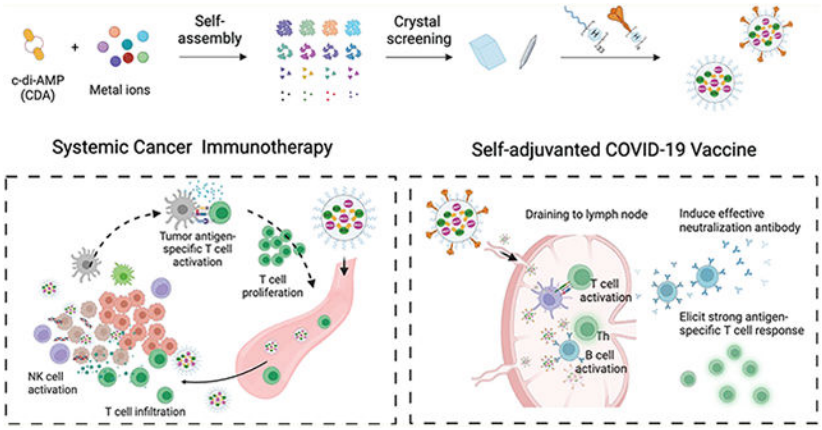

Keywords

STING; coordination nanoparticle; cyclic dinucleotide; cancer immunotherapy; vaccine

The cyclic GMP–AMP synthase stimulator of interferon genes (cGAS-STING) pathway induces the production of type I interferons in response to cytoplasmic DNA and triggers the cascade of adaptive immune responses, thus playing a pivotal role in innate immunity against cancer and infection.[1–5] Cyclic dinucleotides (CDN), the second messenger produced by cGAS, activate STING, and CDN-based STING agonists have emerged as promising agents for cancer immunotherapy and vaccine adjuvants.[3,6–10] However, poor drug-like properties of CDNs, including vulnerability to enzymatic degradation and poor cellular uptake, preclude their systemic administration and clinical efficacy.[11–14] Even with localized injections, CDNs are rapidly cleared, diminishing their bioavailability in target tissues[15]— whether in tumors for cancer immunotherapy or lymph nodes for vaccine applications. These limitations underline the urgent need for the development of CDN delivery systems to realize their therapeutic potential.

Notably, the assembly of coordination supermolecules of CDNs by metal ions has shown promise for the formulation of STING agonists for local and systemic delivery.[14,16,17] Conventional methods for producing stable coordination polymer-based nanomedicines often require harsh synthesis conditions, emulsion processing, or the application of complex coatings to enhance stability.[18–20] However, the harsh synthesis conditions, including a high temperature[21,20] and the use of organic solvents,[22] can pose challenges for their use in the pharmaceutical formulation of biomolecules, such as CDNs and proteins. Furthermore, the nanoemulsion-assisted synthesis[16,19] or complex coating processes[14,16,20] can introduce complexities during the scale-up process and may subject the biomolecules to stress, potentially affecting their functionality or integrity. Thus, there is a need for a gentle, aqueous synthesis approach for producing coordination polymer nanomedicine that imparts good stability and biocompatibility, potentially streamlining the production, scale-up, and translation of these nanoparticles.[23,24] Such a strategy could also broaden the utility of coordination polymer nanomedicine for the formulation of proteins and other biopharmaceuticals.

In this study, we sought to establish a simple yet effective coordination nanoparticle platform for the delivery of CDNs and, when required, co-delivery of proteins (Scheme 1). Our methodology commenced with the screening of aqueous coordination interactions between cyclic di-AMP (CDA) and essential nutritional metal ions. Interestingly, we found that Zn^{2+} and CDA can form unique macro-scale crystal structures, and the addition of Mn^{2+} can transform the crystal shape, resulting in needle-like CDA–Mn–Zn crystals. Furthermore, incorporation of PEGylated polyhistidine can facilitate the formation of homogeneous nanoparticles, which we termed Zinc–Mn–CDN Particle (ZMCP). This nanoparticle system demonstrated good aqueous stability and enabled the systemic delivery of CDA for safe and effective cancer immunotherapy in murine models of cancer. Moreover, the gentle nature of this synthesis method is compatible with the protein formulation. His-tagged COVID-19 spike protein antigens could be assembled onto ZMCP via coordination with a high encapsulation efficacy. The self-adjuvanted ZMCP COVID-19 vaccines induced a potent cellular immune response accompanied by neutralizing antibody response. Overall, we developed an aqueous coordination nanoparticle platform for the co-delivery of CDN and protein, with potential applications in cancer immunotherapy and vaccines. It presents a paradigm of developing translational coordination nanomedicine based on drug–metal ion coordination and expands the applicability of coordination medicine in the formulation and delivery of proteins and other biomolecules.

RESULTS AND DISCUSSION

Crystal forms of drugs may improve their efficacy, solubility, shelf life, and manufacturing.[25] We delved into the coordination behavior of CDN with a range of nutritional metal ions (e.g., Zn^{2+}, Ni^{2+}, Mg^{2+}, Mn^{2+}, Ca^{2+}, Al^{3+}, Cu^{2+}, Fe^{3+}, Fe^{2+}, and Co^{2+}). Among these, Zn^{2+}, Mn^{2+}, Al^{3+}, Cu^{2+}, and Fe^{3+} were observed to form precipitates with CDN in water (Figure 1A–C and Figure S1). Of note, Zn formed macroscale crystal structures with CDN, indicating well-organized coordination behavior (Figure 1C). To further characterize this behavior, we titrated the molar ratio of Zn/CDN and found that Zn formed crystal structures from 1:0.5. Interestingly, Zn-CDN formed rod-like crystals

at low molar ratios (1:0.5 to 1:4) and formed into cubelike crystals when the molar ratio reached 1:8 (Figure 1D). Interestingly, even though Mn-CDN coordination aggregates were amorphous, Mn-doped Zn-CDN (CDA–Zn-Mn) formed needle-like crystals, and their size decreased as more metal ions were added (Figure 1D). As shown in element mapping of CDA–Zn–Mn (Figure S2), Zn and Mn were evenly distributed inside the crystals with a ratio of CDA/Mn/Zn = 3.3:1.2:0.8, which was calculated based on the measurement of P/Mn/Zn. However, these coordination structures were unstable and promptly dissolved in PBS. Consequently, local injection of CDA and CDA–Zn–Mn *in vivo* yielded no difference for STING-dependent cytokine production (Figure S3) and antitumor therapeutic effect (Figure S4). To address these issues, we incorporated histidine$_{33}$-PEG (H33-PEG) to stabilize the coordination and enable their assembly into nanoparticles (Figure 1D). H33-PEG formed homogeneous nanoparticles with CDA and Zn (termed ZCP; Figure 1E, left). However, H33-PEG, Mn, and CDA could form only cluster-like nanoprecipitations (termed MCP; Figure 1E, middle). Fascinatingly, H33-PEG, Zn, Mn, and CDA formed homogeneous nanoparticles (termed ZMCP) with a ratio of CDA/Mn/Zn = 1.6:3.1:5.0 based on element mapping analysis (Figure 1E right, Figure S5). ZMCP exhibited increased stability in PBS, compared to ZCP and MCP (Figure S6). Our subsequent tests evaluated the efficiency of various coordination nanoparticles to activate bone-marrow-derived dendritic cells (BMDCs). ZMCP induced the highest level of CD80 and CD86 costimulatory markers on BMDCs, compared with soluble forms of CDA with or without metal ions or control nanoparticles formed without Zn^{2+} or Mn^{2+} (Figure 1F). These data suggest that ZMCP exhibiting aqueous stability and Mn-mediated potentiation of STING activation[14,26,27] is a promising platform for immune activation.

We further characterized the properties of ZMCP and examined its interactions and behaviors in cellular environments. ZMCP exhibited an average size of 88 ± 20 nm, PDI = 0.2, and a nearly neutral surface charge, as revealed by DLS size and zeta potential measurements (Figure 2A,B). ZMCP released ~60% of CDA and Mn over 10 h in PBS, followed by a slower rate of release (Figure 2C). In contrast, a minimal amount of Zn was released during the 50 h window, indicating that Zn was firmly coordinated within ZMCP. This behavior aligns well with our observation that the morphology of ZMCP more closely resembled ZCP than MCP (Figure 1E), possibly due to the robust coordination between Zn^{2+} and imidazole groups. This coordination mechanism is akin to the mineralization of histidine-rich protein by Zn^{2+} in hard bite parts of marine worms and arthropods.[28] A cell uptake study revealed that ZMCP markedly improved the intracellular delivery of the CDN STING agonist (Figure 2D). It has been reported that polyhistidine can facilitate endosomal escape after being positively charged in the acidic environment of the endosomes, leading to the rupture of the membrane by a proton sponge effect.[29–31] We confirmed this property of ZMCP by a hemolysis assay using red blood cells incubated with ZMCP or H33-PEG at various pH levels. ZMCP did not induce hemolysis at pH 7.4 or 6, but ZMCP and H33-PEG induced substantial hemolysis at pH 5 (Figure 2E), a pH level akin to that of late endosomes and lysosomes. We next examined the functional impact of ZMCP treatment on BMDCs. ZMCP induced BMDCs to produce proinflammatory cytokines and chemokines including IFN-β, TNF-α, CXCL-9, and CXCL-10 (Figure 2F). Overall, ZMCP is an effective intracellular delivery system that increases the cellular uptake of STING

agonists, drives endosomal escape, augments DC activation, and promotes the secretion of inflammatory cytokines and chemokines (Figure 2G).

Next, we evaluated the antitumor efficacy of ZMCP after intratumoral (I.T.) treatment. Given the comparable performance of CDA and CDA–Zn–Mn *in vitro* (Figure 1F) and *in vivo* (Figures S3 and S4), we chose CDA as our control to assess the therapeutic efficacy of ZMCP in a subcutaneous (S.C.) CT26 colon tumor model. First, we assessed the effect of ZMCP on the production of proinflammatory cytokines and chemokines. I.T. injection of ZMCP containing 5 μg of CDA led to a significant increase in TNF-α and CXCL-10 at 6 h postinjection, compared with free CDA (Figure 3A,B). Additionally, compared with free CDA, ZMCP significantly increased the tumor antigen-specific CD8+ T cell responses, as analyzed by AH1-tetramer staining on PBMCs taken on day 18 posttumor inoculation (Figure 3C). From a therapeutic perspective, ZMCP treatment resulted in significant inhibition of tumor growth compared with free CDA treatment (Figure 3D,E). This therapeutic benefit was further underscored by the extended survival of ZMCP-treated mice compared with CDA-treated mice (Figure 3F). After I.T. administration, ZMCP was retained significantly longer in the tumor tissues compared to free CDN control (Figure S7), leading to higher drug bioavailability and improved immune activation in the tumor microenvironment. Indeed, ZMCP therapy significantly increased the intratumoral infiltration of CD8+ T cells, especially AH1 antigen-specific CD8+ T cells, and there was a trend for a higher number of DCs in the tumor and NK cell activation in tumor-draining lymph nodes after ZMCP therapy, compared with free CDA (Figure 3G,H, Figure S8). As another control, we compared ZMCP therapy to CDA–Zn–Mn. ZMCP I.T. therapy with 20 μg completely eradicated CT26 tumors in 100% of mice, significantly outperforming the equivalent dose of CDA–Zn–Mn I.T. therapy (Figure S9). In summary, I.T. injection of ZMCP effectively induced antitumor immune responses and improved the therapeutic effect of the CDN STING agonist.

Systemic administration of STING agonists would offer notable advantages for the treatment of metastatic cancer and clinical translation. So, we next evaluated the therapeutic potential of systemic ZMCP therapy. Mice bearing established CT26 tumors were treated intravenously (I.V.) with 20 μg of CDA either in a free form or in ZMCP on days 11, 14, 17, and 21 (Figure 4A). Compared with soluble CDA, ZMCP significantly increased the serum levels of TNF-α and CXCL-10 (Figure 4B), suggesting a more robust STING activation. ZMCP I.V. therapy led to a marked suppression of CT26 tumor progression and extended animal survival, whereas free CDA therapy had a minimal therapeutic effect (Figure 4C–E). The drug distribution study performed at 24 h post-I.V. injection showed that ZMCP significantly increased CDN accumulation in tumor and spleen (Figure S10), which may have contributed to the systemic and intratumoral immune activation. Flow cytometry analysis performed on day 27 showed that ZMCP I.V. therapy significantly expanded NK cells in PBMCs, induced high NK cell activation in tumor-draining lymph nodes, promoted NK cell infiltration and central memory CD4+ T cells in tumor, and increased the frequency of CD45+ immune cells and CD8+ T cells with high expression of CD107a, indicating activated CD8+ T cells in the spleen (Figure 4F–L).

In a more challenging scenario, we examined ZMCP's performance in an aggressive B16F10 melanoma model. C57BL/6 mice were inoculated with 3×10^5 B16F10 tumor cells on day 0, and after large (>100 mm^3) tumors were established, mice were treated I.V. with 20 μg of CDA either in a free form or in ZMCP on days 11, 14, 17, and 20 (Figure 5A). ZMCP significantly increased the serum levels of STING activation-associated TNF-α and CXCL-10 (Figure 5B). Flow cytometry analysis of the spleen on day 26 showed that ZMCP I.V. therapy significantly expanded NK cells, induced the activation of NK cells and CD8+ T cells, and increased the ratio of antitumor M1 macrophages to pro-tumoral M2 macrophages (Figure 5C–F). Moreover, ZMCP I.V. therapy also significantly increased intratumoral infiltration of NK cells, CD8+ T cells, and CD4+ T cells (Figure 5G–J). In alignment with these findings, B16F10 tumor growth was effectively inhibited and animal survival was significantly increased by the ZMCP therapy (Figure 5K,L). Moreover, antitumor efficacy of ZMCP was further improved when we combined the ZMCP therapy with an anti-PD-1 IgG immune checkpoint blockade in the setting of either local I.T. treatment or systemic I.V. treatment (Figure S11). Altogether, these results show that ZMCP is an effective formulation for the systemic delivery of a STING agonist for mono or combinational immunotherapy of cancer.

STING agonists have garnered attention as a potent adjuvant for vaccines against cancer and infectious pathogens.[9,32] Building on this, we explored the potential of ZMCP as a delivery system with adjuvant activity for S.C. vaccination against SARS-CoV-2. The polyhistidine tag (His-tag) is one of the widely used protein tags of recombinant proteins and is known for its ability to coordinate with metal cations. This can facilitate the loading of various His-tagged proteins into ZMCP. To test this idea, we introduced a 6× His-tag to the spike protein receptor binding domain (RBD), the key binding interface that the SARS-CoV-2 virus uses to initiate membrane fusion,[33] and incorporated this into the one-pot synthesis reaction with ZMCP (Figure 6A). As shown in Figure 6B, over 87% of RBD was efficiently encapsulated in ZMCP, as determined by SDS-PAGE analysis. Next, we tested the vaccine response of ZMCP-RBD in Balb/c mice. After three S.C. vaccinations with a two-week interval, ZMCP-RBD evoked higher anti-RBD IgG and IgG1 antibody titers, compared with a soluble mixture of RBD+CDA+Zn+Mn, RBD+CDA, or RBD+ clinically used Alum adjuvant (Figure 6C). There was a marked increase in B-cell germinal center formation in the draining lymph nodes (dLN) after ZMCP-RBD vaccination (Figure 6D), indicating robust B-cell activation and differentiation induced by ZMCP-RBD. Importantly, antibodies elicited by ZMCP-RBD showed a strong neutralizing effect against pseudotyped SARS-CoV-2 in a viral neutralization assay (Figure 6E). Notably, ZMCP-RBD also stimulated an effective cellular immune response. Mice vaccinated three times with ZMCP-RBD exhibited a strong and broad T-cell response to RBD, with a significant IFN-γ T-cell response to $RBD_{438–458}$ and $RBD_{450–473}$ epitopes, as shown by a splenocyte ELISPOT assay (Figure S12). Even with just a two-dose immunization regimen, ZMCP-RBD induced a significantly higher IFN-γ T-cell response to $RBD_{438–458}$ and $RBD_{450–473}$ (Figure 6F), compared with RBD+CDA+Zn+Mn, RBD+CDA, or RBD+ clinically used Alum adjuvant. This further confirms the effectiveness of ZMCP-RBD in activating the cellular immunity against SARS-CoV2. Visualization of drug trafficking indicated that ZMCP improved CDN retention at the injection site and enhanced LN accumulation, compared with the free form of CDN that

diffused to systemic circulation soon after S.C. administration (Figure S13). This indicates that ZMCP is a promising vaccine delivery system that could home to dLNs after S.C. administration, promoting antigen delivery and presentation, priming B-cell germinal center formation, and leading to strong antigen-specific humoral and cellular immune responses.

Following the promising results obtained with ZMCP-RBD, we further explored the potential of ZMCP as a delivery platform for spike protein subunit 1 (S1) from SARS-CoV-2 (Figure 7). Similar to the process used for ZMCP-RBD, we formulated ZMCP-S1 via a one-pot synthesis, where CDA, H33-PEG20k, Zn^{2+}+Mn^{2+}, and S1–H6 were simply mixed sequentially (Figure 7A). S1 was efficiently encapsulated in ZMCP-S1 with over 76% encapsulation efficacy, as shown by the SDS-PAGE analysis after lysis of the particles (Figure 7B). Mice vaccinated with ZMCP-S1 induced potent S1-specific humoral immune responses. Interestingly, both ZMCP-S1 and a soluble mixture of S1+CDA+Zn+Mn elicited a strong IgG and IgG1 antibody response against S1, with higher antibody titers than the admixture of S1+CDA or S1+ Alum (Figure 7C). Importantly, antibodies elicited by ZMCP-S1 exhibited significantly stronger neutralizing activity against SARS-CoV-2 *in vitro*, compared with antibodies induced by soluble formulations of S1+CDA+Zn+Mn or S1+CDA (Figure 7D). Moreover, ZMCP-S1 promoted significantly higher B cell germinal center formation in dLNs, compared with S1+CDA or S1+CDA+Zn+Mn (Figure 7E), suggesting more mature B-cell activation and differentiation induced by ZMCP-S1. Overall, ZMCP is a promising vaccine delivery system that elicits robust germinal center formation and antiviral neutralizing antibody responses. These results highlight the versatility of ZMCP as a self-adjuvanted vaccine platform that allows for facile formulation of protein antigens and induction of robust antiviral immune responses.

Collectively, our findings demonstrate the effectiveness of ZMCP in delivering CDN for cancer immunotherapy, as well as in the codelivery of CDN and protein antigens for vaccination against infectious pathogens. In addition, ZMCP treatments exhibited excellent safety profiles after administration via intratumoral or intravenous routes. Based on the animal body weight, serum chemistry, and histological analysis of major organs, we have not observed any overt signs of systemic toxicity (Figure S14). The observed safety could be attributed to the minimal metal ion doses that were used: about 0.1 mg/kg of Mn and 0.53 mg/kg of Zn were used for I.V. injection, and about 0.025 mg/kg of Mn and 0.13 mg/kg of Zn were used for I.T. injection. For comparison, the LD50 of $MnCl_2$ in mice is 1715 mg/kg and average daily diet consumption of Mn in adults is up to 10 mg.[34] The oral LD50 of Zn in rats is close to 3000 mg/kg, and the recommended daily consumption of Zn in adults is 15 mg.[35,36] Regarding its applicability as a self-adjuvanted vaccine delivery platform, no signs of toxicity or intolerance were identified either. Histological analysis of major organs did not reveal any anomalies after 3 doses of vaccination (Figure S15). Note that we used 5 μg of CDA, 4.17 μg of Mn, and 4.93 μg of Zn per dose of ZMCP vaccine. These findings suggest that ZMCP holds significant promise as an effective and safe platform for cancer immunotherapy and vaccination against infectious pathogens.

CONCLUSION

In summary, we establish a streamlined yet effective coordination nanomedicine platform for drug and vaccine delivery. This innovation is rooted in our exploration of the distinct coordination dynamics between drugs and metal ions, complemented with polyhistidine PEG to bolster the coordination and facilitate nanoparticle self-assembly. This current approach is both gentle and straightforward, accommodating the formulation of proteins and other biomolecular structures. In the context of cancer therapeutics, ZMCP effectively delivered CDA to tumor tissues, resulting in a strong antitumor immune response, inhibition of tumor growth, and extension of survival after both local and systemic injection. In terms of vaccine delivery, ZMCP has shown substantial potential as a carrier for SARS-CoV-2 antigen proteins, leading to the generation of self-adjuvanted vaccines. Vaccines based on ZMCP stimulated strong humoral and cellular immune responses, showing the potential for vaccines tailored to combat emerging infectious diseases. Overall, this work introduces a paradigm of translational coordination nanomedicine development, leveraging drug–metal ion synergy and broadens the horizons of coordination medicine for the formulation and delivery of biomolecules.

EXPERIMENTAL SECTION

Screening of CDN-Metal Ion Coordination Structures.

c-di-AMP (CDA) was obtained from Invivogen and dissolved in water to obtain a 2 mg/mL solution. $ZnCl_2$, $MgCl_2$, $MnCl_2$, $CaCl_2$, $Al_2(SO_4)_3$, $CuCl_2$, $FeCl_2$, $FeCl_3$, $NiCl_2$, and $CoCl_2$ (Sigma-Aldrich) were each dissolved in water to prepare a 100 mM solution. To screen for metal ions that could coordinate with CDA, 5 or 10 equiv (n/n) of metal ions was added to 2 mg/mL CDA solution. The mixture solution was incubated for 2 h at room temperature. The resulting CDN–metal coordination structures were observed under an EVOS microscope. The degree of precipitation of CDN–metal solution was assessed by measuring absorbance at OD 450 nm, OD 500 nm, and OD 600 nm after subtracting the background absorbance. The loading efficacy of CDN in the coordination structure was measured by quantifying CDN in the supernatant and pellets after centrifugation at 10 000*g* for 15 min.

Synthesis and Characterization of ZMCP, ZCP, and MCP.

ZMCP was prepared by adding premixed Zn^{2+}+Mn^{2+} solution to premixed CDA and H33-PEG20k solution with stirring. Briefly, an equal volume of 10 mg/mL H33-PEG was added dropwise to 2 mg/mL CDA solution with continuous stirring. Then, 20 equiv of Zn^{2+}+Mn^{2+} solution was added to CDA (1 equiv) and H33-PEG20k mixture under stirring and reacted for 12 h. ZMCP was isolated by centrifuge or centrifugal ultrafiltration (100 kDa).

ZCP or MCP was prepared by adding Zn^{2+} or Mn^{2+} solution to premixed CDA and H33-PEG20k solution with stirring. Briefly, an equal volume of 10 mg/mL H33-PEG20k was added dropwise to 2 mg/mL of CDA solution with continuous stirring. Then, 20 equiv of Zn^{2+} or Mn^{2+} solution was added to CDA (1 equiv) and H33-PEG20k mixture under stirring and reacted for 12 h. ZCP or MCP was isolated by centrifuge or centrifugal ultrafiltration (100 kDa).

ZMCP-RBD or ZMCP-S1 was prepared by adding premixed Zn^{2+}+Mn^{2+} solution to a premixed solution of CDA, H33-PEG20k, and RBD or S1 antigen proteins (Acro Biosystems) with stirring. Briefly, a designated amount of antigen protein was added to the solution of 1 mg/mL of CDA and 5 mg/mL of H33-PEG20k with continuous stirring. Then, 20 equiv of Zn^{2+}+Mn^{2+} solution was added to the mixture solution of CDA (1 equiv), H33-PEG20k, and antigen protein under stirring and reacted overnight at 4 °C. The formulation was used for injection without further purification.

Loading of CDA in ZMCP was quantified by the UV absorbance at 260 nm after lysis. Loading of Mn^{2+} in ZMCP was quantified by inductively coupled plasma-mass spectrometry (PerkinElmer Nexion 2000 ICP-MS). Loading of proteins was quantified by SDS-PAGE. The size and surface charge of ZMCP were measured by a Zetasizer (Nano ZSP, Malvern, UK). The elemental mapping of a CDA:Mn:Zn crystal and ZCMP were performed on a Thermo Fisher Talos F200X G2 TEM. The morphology of ZMCP, ZCP, and MCP was observed by transmission electron microscopy (TEM). All images were acquired on a JEM 1200EX electron microscope (JEOL USA, Peabody, MA) equipped with an AMT XR-60 digital camera (Advanced Microscopy Techniques Corp., Woburn, MA).

In Vitro Release Analysis.

The drug release profiles of formulations were studied with a Slide-A-Lyzer MINI Dialysis Device, 20 kDa MWCO (Thermo Scientific). Briefly, 0.5 mL of formulation solution was filled in the cup with regenerated cellulose membrane, and 14 mL of release buffer (PBS) was put in the tube. After the dialysis cup was inserted into the conical tube and capped, the device was incubated at 37 °C under continuous shaking (200 rpm). At the indicated time points, 300 μL of release media were collected and an equal amount of fresh PBS was refilled. The concentration of CDA in the release medium was analyzed by HPLC. And the concentration of Zn and Mn in the release medium was analyzed by ICP-MS. Finally, the release amount of CDA over time was calculated based on the CDA concentration in the release buffer, volume of buffer, and the total CDA loading amount.

In Vitro Evaluation of BMDC Activation, Cellular Uptake, and STING Activation.

BMDCs were prepared as described previously.[37] Briefly, bone marrow was harvested and plated in bacteriological Petri dishes with GM-CSF-containing culture media. The cell culture media were refreshed on days 3, 6, and 8. After 8 days of differentiation, the BMDCs were harvested for use. To observe BMDC activation, 1×10^6/well BMDCs seeded in 12-well plates were incubated for 24 h with ZMCP or related controls containing 5 μM CDA or/and 20 μM Mn or/and 43.5 μM Zn. Treated BMDCs were harvested, washed with 1% BSA in PBS, incubated with anti-CD16/32 at room temperature, and stained on ice with fluorophore-labeled antibodies against CD11c, CD80, and CD86. Cells were then washed twice using 1% BSA in PBS, resuspended in 2 μg/mL DAPI solution, and analyzed by flow cytometry (Ze 5, Bio-Rad, USA).

To visualize and quantify cellular uptake of the STING agonist, fluorophore-labeled CDN, CDG-Dy547 (Biolag, Bremen, German), was admixed with CDA (1:10, n/n) to prepare ZMCP following the same synthesis procedure as ZMCP mentioned above. Loading of

CDG-Dy547 in ZMCP was quantified by the absorbance at 550 nm. BMDCs were seeded at 1×10^6 cells on 35 mm Petri dishes (MatTek Corp., Ashland, MA) and incubated with CDG-Dy547 in free form or in CDG-Dy547@ZMCP for 6, 12, or 24 h. For confocal imaging, cells were washed 3 times with PBS, incubated with 50 nM LysoTracker green DND-99 (Invitrogen) for 30 min at 37 °C to stain lysosomes, and then imaged using a confocal microscope (Nikon A1). For cellular uptake quantification, cells were harvested and washed with 1% BSA in PBS. The fluorescence of CDG-Dy547 was analyzed by flow cytometry (Ze 5, Bio-Rad, USA).

To measure STING activation of CDA in free form or in ZMCP, 1×10^5/well BMDCs were seeded in a 96-well plate and incubated with a serial amount of CDA in free form or in ZMCP. After 24 h of incubation at 37 °C and 5% CO_2, the supernatants were collected for ELISA assay of cytokines at the Cancer Center Immunology Core of the University of Michigan.

In Vivo Cancer Immunotherapy.

All animals were cared for following federal, state, and local guidelines. All work performed on animals was in accordance with and approved by the Institutional Animal Care and Use Committee (IACUC) at the University of Michigan, Ann Arbor. For the CT26 murine tumor model, female BALB/c mice of age 6–8 weeks (Jackson Laboratories) were inoculated with the indicated number of CT26 colon cancer cells S.C. on the right back flank. For the B16F10 tumor model, C57BL/6 mice (Jackson Laboratory) were inoculated with the indicated number of B16F10 cells S.C. on the right flank. Tumor-bearing mice were randomly assigned to different treatment groups. Tumor size and survival were monitored every 2–4 days. Tumor size was calculated based on the equation volume = length × width^2 × 0.5. Animals were euthanized when the tumor reached 1.5 cm in diameter or when the animals became moribund with severe weight loss or unhealing ulceration. At indicated time points, the cytokine levels in serum were measured by an ELISA assay in the Cancer Center Immunology Core of the University of Michigan. The percentages of tumor antigen-specific CD8+ T cells among PBMCs were analyzed using the tetramer staining assay as described previously with an AH1 peptide-MHC tetramer (H-2Kb-restricted AH1 (SPSYVYHQF); the NIH Tetramer Core Facility, Atlanta, GA).[14,38] An ELISPOT assay was performed with PBMCs from the treated mice, as described previously.[39]

In Vivo Immune Response Analysis.

T cell phenotypic and functional assessment in PBMCs were analyzed. Briefly, PBMCs were collected after red blood cells were removed by ACK lysis buffer. The Fc receptor of PBMCs was blocked with the CD16/32 antibody for 10 min. To analyze the tumor antigen-specific $CD8^+$ T cells response and T cell memory phenotype, cell pellets were first stained with a PE-tagged AH1 peptide-MHC tetramer, and then further stained with BV605-CD8a rat antimouse (Clone: 53–6.7(RUO), BioLegend). Stained cells were incubated with DAPI prior to flow cytometry analysis (Ze5, Bio-Rad).

Tumor tissues, tumor-draining lymph nodes, or spleen were analyzed as described before.[38] Tumor tissues were excised at preset time points and cut into small pieces, which were

treated additionally with collagenase type IV (1 mg/mL) and DNase I (0.1 mg/mL) under gentle shaking. After 30 min, the cell suspension was filtered through a 70-μm strainer. The cells were washed with FACS buffer and blocked with the CD16/32 antibody. Cells were then stained with the designated antibodies: FITC-Antimouse CD45 Antibody (Clone: 30-F11, BioLegend) or APC-Cy7-Antimouse CD45 Antibody (Clone: 30-F11, BioLegend), APC-CD8a rat antimouse (Clone: 53–6.7(RUO) or BV605-Antimouse CD8a Antibody (Clone: 53–6.7, BioLegend), BD Biosciences), FITC antimouse NK-1.1 Antibody (Clone: S17016D, BioLegend), APC-Antimouse CD107a Antibody (1D4B, BioLegend), and PE-AH1 Tetramer (NIH). Stained cells were incubated with DAPI prior to flow cytometry analysis (Ze5, Bio-Rad).

In Vivo Drug Distribution Analysis.

To analyze *in vivo* biodistribution of the CDN STING agonist, CDG-Dy547 (Biolag, Bremen, Germany) or CDG-Cy7 (Biolag, Bremen, Germany) was admixed with CDA (1:10, n/n) to prepare CDG-Dy547@ZMCP or CDG-Cy7@ZMCP following the same synthesis procedure as that of ZMCP mentioned above. The loading of CDG-Dy547 and CDG-Cy7 was quantified by absorbance at 550 or 750 nm. To quantify drug retention at the tumor site after intratumoral injection, CDG-Cy7 in the free form or in ZMCP was injected into tumors. Mice were imaged by IVIS at different time points (10 min, 1 h, 4 h, 6 h, 16 h, 24 h) and the fluorescence signal of CDG-Cy7 in tumors was measured accordingly. To quantify the biodistribution of ZMCP after I.V. administration, CDG-Cy7 in the free form or in ZMCP was injected I.V. Mice were euthanized 24 h postinjection, and the fluorescence intensity in major organs was measured accordingly.

In Vivo Immunization with COVID-19 Vaccine.

Balb/c mice were vaccinated three times at the tail base in two-week intervals. Two weeks after each vaccination and four and eight weeks after the last vaccination, sera were collected for antibody titer measurement by ELISA. In a separate study, spleens were harvested 1 week after the last vaccination for an ELISPOT assay. For the ELISA assay, 96-well plates were pretreated overnight with 0.1 μg of RBD (dissolved in carbonate–bicarbonate buffer, pH 9.6) per well. After removing RBD, wells were washed three times with wash solution and further incubated with blocking solution (1% BSA in PBS) for 2 h in RT, then washed three times with wash solution (0.05% Tween 20 in PBS). Next, sera samples were placed on the plates. Sera samples were serially diluted by 1:4 or 1:5 six times with a starting dilution of 1:100. After incubating the samples for 1 h in RT, samples were removed, followed by three rounds of washing. Next, 1:1000-diluted HRP-conjugated antimouse IgG antibodies (ab6728; Abcam) were added and incubated for 1 h in RT. After the incubation, antibodies were removed, and the wells were washed four times with wash solution, then substrate solution (Ultra TMB-ELISA; Thermo Scientific) was added and incubated for 10 min or until the reacting solution colors were well developed in RT. The reaction was stopped by adding 1 M H_2SO_4, then the plates were read at a wavelength of 450 nm. To study viral neutralization capacity, sera of ZMCP-RBD immunized mice were collected on weeks 6 and 14 and tested for neutralizing activity against SARS-CoV-2 spike pseudotyped virus in HEK293T-ACE2 cells.[40] Furthermore, sera of ZMCP-S1 immunized

mice were collected on weeks 6 and 14 and tested for neutralizing activity against SARS-CoV-2 (USA-WA1/2020) infection in Vero E6 cells.[41]

ELISPOT Assay.

A day before spleen harvest, a 96-well ELISPOT plate was coated with the captured antibody (anti-IFN-γ antibody). After overnight incubation at 4 °C, wells were washed with blocking solution, followed by incubation with blocking solution for 2 h. Next the blocking solution was removed, and RBD peptides were added to the wells in 10 μg/mL concentration. Spleens were harvested 1 week after the last vaccination. Splenocytes were counted, and 2×10^5 cells were seeded in each well of the 96-well ELISPOT plate containing the RBD peptides (10 μg/mL). Ionomycin and phorbol myristate acetate were employed as a positive control. After 18 h, IFN-γ spots were detected with biotinylated detection antibodies, followed by streptavidin–horseradish peroxidase and a 3-amino-9-ethylcarbazole substrate kit. The IFN-γ spot number and size were measured in the Cancer Center Immunology Core at the University of Michigan.

Statistical Analysis.

The results are expressed as means ± SEM. A one-way or two-way ANOVA, followed by Bonferroni's multiple comparisons post hoc test, was used for testing differences among groups. Data were approximately normally distributed, and variance was similar between the groups. Experiments were repeated multiple times as independent experiments as indicated in the figure captions. Shown in the figure is a complete data set from one representative, independent experiment. No samples were excluded from analysis. Statistical significance is indicated as $*P < 0.05$, $**P < 0.01$, $***P < 0.001$, and $****P < 0.0001$. GraphPad Prism 8.0 (GraphPad Software, La Jolla, CA) was used for statistical analyses.

Supplementary Material

Refer to Web version on PubMed Central for supplementary material.

ACKNOWLEDGMENTS

This work was supported in part by NIH (R01DE030691, R01DE031951, R01DK125087, R01CA271799, R01NS122536, R01DE026728, R44CA281497), the University of Michigan Rogel Cancer Center Support Grant (P30CA46592), and the Frankel Innovation Initiative at the University of Michigan. We acknowledge Angela Dial at Michigan Element Analysis Lab for Mn biodistribution analysis and Joel Whitfield at the University of Michigan Cancer Center Immunology Core for ELISA analysis. We also thank the University of Michigan Flow Cytometry Core, the ULAM (Unit for Laboratory Animal Medicine), In Vivo Animal Core (IVAC), and the University of Michigan Microscope Imaging Core for technical assistance. The authors acknowledge the financial support of the University of Michigan College of Engineering and technical support from the Michigan Center for Materials Characterization. We acknowledge the NIH Tetramer Core Facility (contract HHSN272201300006C) for the provision of MHC-I tetramers. The following reagent was deposited by the Centers for Disease Control and Prevention and obtained through BEI Resources, NIAID, NIH: SARSRelated Coronavirus 2, Isolate hCoV-19/USA-WA1/2020, NR-52281.

The authors declare the following competing financial interest(s): A patent application for ZMCP has been filed, with J.J.M., X.S., X.H., and C.P. as inventors. J.J.M. declares financial interests for board membership, as a paid consultant, for research funding, and/or as an equity holder in Saros Therapeutics and EVOQ Therapeutics. The University of Michigan has a financial interest in EVOQ Therapeutics. Y.L.L declares financial interests for board membership and/or as an equity holder in Saros Therapeutics. X.S. is an employee and shareholder in Editas Medicine.

REFERENCES

(1). Wu J; Sun L; Chen X; Du F; Shi H; Chen C; Chen ZJ Cyclic GMP-AMP is an endogenous second messenger in innate immune signaling by cytosolic DNA. Science 2013, 339 (6121), 826–830. [PubMed: 23258412]

(2). Sun L; Wu J; Du F; Chen X; Chen ZJ Cyclic GMP-AMP synthase is a cytosolic DNA sensor that activates the type I interferon pathway. Science 2013, 339 (6121), 786–791. [PubMed: 23258413]

(3). Gajewski TF; Higgs EF Immunotherapy with a sting. Science 2020, 369 (6506), 921–922. [PubMed: 32820113]

(4). Ablasser A; Chen ZJ cGAS in action: Expanding roles in immunity and inflammation. Science 2019, 363 (6431). DOI: 10.1126/science.aat8657

(5). Ishikawa H; Ma Z; Barber GN STING regulates intracellular DNA-mediated, type I interferon-dependent innate immunity. Nature 2009, 461 (7265), 788–792. [PubMed: 19776740]

(6). Corrales L; Glickman LH; McWhirter SM; Kanne DB; Sivick KE; Katibah GE; Woo S-R; Lemmens E; Banda T; Leong JJ; Metchette K; Dubensky TW; Gajewski TF Direct activation of STING in the tumor microenvironment leads to potent and systemic tumor regression and immunity. Cell reports 2015, 11 (7), 1018–1030. [PubMed: 25959818]

(7). Curran E; Chen X; Corrales L; Kline DE; Dubensky TW; Duttagupta P; Kortylewski M; Kline J STING Pathway Activation Stimulates Potent Immunity against Acute Myeloid Leukemia. Cell Reports 2016, 15 (11), 2357–2366. [PubMed: 27264175]

(8). Junkins RD; Gallovic MD; Johnson BM; Collier MA; Watkins-Schulz R; Cheng N; David CN; McGee CE; Sempowski GD; Shterev I; McKinnon K; Bachelder EM; Ainslie KM; Ting JP-Y A robust microparticle platform for a STING-targeted adjuvant that enhances both humoral and cellular immunity during vaccination. J. Controlled Release 2018, 270, 1–13.

(9). Wang J; Li P; Yu Y; Fu Y; Jiang H; Lu M; Sun Z; Jiang S; Lu L; Wu MX Pulmonary surfactant-biomimetic nanoparticles potentiate heterosubtypic influenza immunity. Science 2020, 367 (6480). DOI: 10.1126/science.aau0810.

(10). Chin EN; Yu C; Vartabedian VF; Jia Y; Kumar M; Gamo AM; Vernier W; Ali SH; Kissai M; Lazar DC; Nguyen N; Pereira LE; Benish B; Woods AK; Joseph SB; Chu A; Johnson KA; Sander PN; Martinez-Pena F; Hampton EN; Young TS; Wolan DW; Chatterjee AK; Schultz PG; Petrassi HM; Teijaro JR; Lairson LL Antitumor activity of a systemic STING-activating non-nucleotide cGAMP mimetic. Science 2020, 369 (6506), 993–999. [PubMed: 32820126]

(11). Meric-Bernstam F; Werner T; Hodi S; Messersmith W; Lewis N; Talluto C; Dostalek M; Tao A; McWhirter S; Trujillo D; Luke JJ Phase I dose-finding study of MIW815 (ADU-S100), an intratumor STING agonist, in patients with advanced solid tumors or lymphomas. Annual Meeting of the Society for Immunotherapy of Cancer Washington, DC 2018, 462–3.

(12). Ramanjulu JM; Pesiridis GS; Yang J; Concha N; Singhaus R; Zhang S-Y; Tran J-L; Moore P; Lehmann S; Eberl HC; Muelbaier M; Schneck JL; Clemens J; Adam M; Mehlmann J; Romano J; Morales A; Kang J; Leister L; Graybill TL; Charnley AK; Ye G; Nevins N; Behnia K; Wolf AI; Kasparcova V; Nurse K; Wang L; Puhl AC; Li Y; Klein M; Hopson CB; Guss J; Bantscheff M; Bergamini G; Reilly MA; Lian Y; Duffy KJ; Adams J; Foley KP; Gough PJ; Marquis RW; Smothers J; Hoos A; Bertin J Design of amidobenzimidazole STING receptor agonists with systemic activity. Nature 2018, 564 (7736), 439. [PubMed: 30405246]

(13). Pan BS; Perera SA; Piesvaux JA; Presland JP; Schroeder GK; Cumming JN; Trotter BW; Altman MD; Buevich AV; Cash B; Cemerski S; Chang W; Chen Y; Dandliker PJ; Feng G; Haidle A; Henderson T; Jewell J; Kariv I; Knemeyer I; Kopinja J; Lacey BM; Laskey J; Lesburg CA; Liang R; Long BJ; Lu M; Ma Y; Minnihan EC; O'Donnell G; Otte R; Price L; Rakhilina L; Sauvagnat B; Sharma S; Tyagarajan S; Woo H; Wyss DF; Xu S; Bennett DJ; Addona GH An orally available non-nucleotide STING agonist with antitumor activity. Science 2020, 369 (6506), DOI: 10.1126/science.aba6098.

(14). Sun X; Zhang Y; Li J; Park KS; Han K; Zhou X; Xu Y; Nam J; Xu J; Shi X; Wei L; Lei YL; Moon JJ Amplifying STING activation by cyclic dinucleotide-manganese particles for local and systemic cancer metalloimmunotherapy. Nat. Nanotechnol 2021, 16 (11), 1260–1270. [PubMed: 34594005]

(15). Meric-Bernstam F; Sweis RF; Hodi FS; Messersmith WA; Andtbacka RHI; Ingham M; Lewis N; Chen X; Pelletier M; Chen X; Wu J; Dubensky TW; McWhirter SM; Muller T; Nair N; Luke JJ Phase I Dose-Escalation Trial of MIW815 (ADU-S100), an Intratumor STING Agonist, in Patients with Advanced/Metastatic Solid Tumors or Lymphomas. Clinical cancer research 2022, 28 (4), 677–688. [PubMed: 34716197]

(16). Yang K; Han W; Jiang X; Piffko A; Bugno J; Han C; Li S; Liang H; Xu Z; Zheng W; Wang L; Wang J; Huang X; Ting JPY; Fu YX; Lin W; Weichselbaum RR Zinc cyclic di-AMP nanoparticles target and suppress tumours via endothelial STING activation and tumour-associated macrophage reinvigoration. Nat. Nanotechnol 2022, 17 (12), 1322–1331. [PubMed: 36302963]

(17). Palermo G; Spinello A; Saha A; Magistrato A Frontiers of metal-coordinating drug design. Expert Opin Drug Discov 2021, 16 (5), 497–511. [PubMed: 33874825]

(18). Sun W; Li S; Tang G; Luo Y; Ma S; Sun S; Ren J; Gong Y; Xie C Recent Progress of Nanoscale Metal-Organic Frameworks in Cancer Theranostics and the Challenges of Their Clinical Application. Int. J. Nanomedicine 2019, 14, 10195–10207. [PubMed: 32099352]

(19). Liu D; Poon C; Lu K; He C; Lin W Self-assembled nanoscale coordination polymers with trigger release properties for effective anticancer therapy. Nat. Commun 2014, 5, 4182. [PubMed: 24964370]

(20). Liu J; Yang G; Zhu W; Dong Z; Yang Y; Chao Y; Liu Z Light-controlled drug release from singlet-oxygen sensitive nanoscale coordination polymers enabling cancer combination therapy. Biomaterials 2017, 146, 40–48. [PubMed: 28941551]

(21). He S; Wu L; Li X; Sun H; Xiong T; Liu J; Huang C; Xu H; Sun H; Chen W; Gref R; Zhang J Metal-organic frameworks for advanced drug delivery. Acta Pharm. Sin B 2021, 11 (8), 2362–2395. [PubMed: 34522591]

(22). Bustamante EL; Fernandez JL; Zamaro JM Influence of the solvent in the synthesis of zeolitic imidazolate framework-8 (ZIF-8) nanocrystals at room temperature. J. Colloid Interface Sci. 2014, 424, 37–43. [PubMed: 24767495]

(23). Mitchell MJ; Billingsley MM; Haley RM; Wechsler ME; Peppas NA; Langer R Engineering precision nanoparticles for drug delivery. Nat. Rev. Drug Discov 2021, 20 (2), 101–124. [PubMed: 33277608]

(24). van der Meel R; Sulheim E; Shi Y; Kiessling F; Mulder WJM; Lammers T Smart cancer nanomedicine. Nat. Nanotechnol 2019, 14 (11), 1007–1017. [PubMed: 31695150]

(25). Datta S; Grant DJ Crystal structures of drugs: advances in determination, prediction and engineering. Nat. Rev. Drug Discov 2004, 3 (1), 42–57. [PubMed: 14708020]

(26). Wang C; Guan Y; Lv M; Zhang R; Guo Z; Wei X; Du X; Yang J; Li T; Wan Y; Su X; Huang X; Jiang Z Manganese Increases the Sensitivity of the cGAS-STING Pathway for Double-Stranded DNA and Is Required for the Host Defense against DNA Viruses. Immunity 2018, 48 (4), 675–687. [PubMed: 29653696]

(27). Lv M; Chen M; Zhang R; Zhang W; Wang C; Zhang Y; Wei X; Guan Y; Liu J; Feng K; Jing M; Wang X; Liu YC; Mei Q; Han W; Jiang Z Manganese is critical for antitumor immune responses via cGAS-STING and improves the efficacy of clinical immunotherapy. Cell Res. 2020, 30 (11), 966–979. [PubMed: 32839553]

(28). Broomell CC; Khan RK; Moses DN; Miserez A; Pontin MG; Stucky GD; Zok FW; Waite JH Mineral minimization in nature's alternative teeth. J. R Soc. Interface 2007, 4 (12), 19–31. [PubMed: 17015290]

(29). Wojnilowicz M; Glab A; Bertucci A; Caruso F; Cavalieri F Super-resolution Imaging of Proton Sponge-Triggered Rupture of Endosomes and Cytosolic Release of Small Interfering RNA. ACS Nano 2019, 13 (1), 187–202. [PubMed: 30566836]

(30). Shae D; Becker KW; Christov P; Yun DS; Lytton-Jean AKR; Sevimli S; Ascano M; Kelley M; Johnson DB; Balko JM; Wilson JT Endosomolytic polymersomes increase the activity of cyclic dinucleotide STING agonists to enhance cancer immunotherapy. Nat. Nanotechnol 2019, 14 (3), 269–278. [PubMed: 30664751]

(31). Yang Y; Xu L; Zhu W; Feng L; Liu J; Chen Q; Dong Z; Zhao J; Liu Z; Chen M One-pot synthesis of pH-responsive charge-switchable PEGylated nanoscale coordination polymers for improved cancer therapy. Biomaterials 2018, 156, 121–133. [PubMed: 29195181]

(32). Van Herck S; Feng B; Tang L Delivery of STING agonists for adjuvanting subunit vaccines. Adv. Drug Deliv. Rev 2021, 179, 114020. [PubMed: 34756942]

(33). Tai W; He L; Zhang X; Pu J; Voronin D; Jiang S; Zhou Y; Du L Characterization of the receptor-binding domain (RBD) of 2019 novel coronavirus: implication for development of RBD protein as a viral attachment inhibitor and vaccine. Cell Mol. Immunol 2020, 17 (6), 613–620. [PubMed: 32203189]

(34). Lewis RTR Registry of Toxic Effects of Chemical Substances; US Department of Health and Human Services, National Institute for Occupational Safety and Health, 1980; Vol. 1.

(35). Plum LM; Rink L; Haase H The essential toxin: impact of zinc on human health. Int. J. Environ. Res. Public Health 2010, 7 (4), 1342–65. [PubMed: 20617034]

(36). Igic PG; Lee E; Harper W; Roach KW Toxic effects associated with consumption of zinc. Mayo Clin Proc 2002, 77 (7), 713–6. [PubMed: 12108610]

(37). Lutz MB; Kukutsch N; Ogilvie AL; Rossner S; Koch F; Romani N; Schuler G An advanced culture method for generating large quantities of highly pure dendritic cells from mouse bone marrow. J. Immunol Methods 1999, 223 (1), 77–92. [PubMed: 10037236]

(38). Kuai R; Yuan W; Son S; Nam J; Xu Y; Fan Y; Schwendeman A; Moon JJ Elimination of established tumors with nanodisc-based combination chemoimmunotherapy. Sci. Adv 2018, 4 (4), No. eaao1736.

(39). Kuai R; Sun X; Yuan W; Xu Y; Schwendeman A; Moon JJ Subcutaneous Nanodisc Vaccination with Neoantigens for Combination Cancer Immunotherapy. Bioconjug Chem 2018, 29 (3), 771–775. [PubMed: 29485848]

(40). Xu C; Dobson HE; Yu M; Gong W; Sun X; Park KS; Kennedy A; Zhou X; Xu J; Xu Y; Tai AW; Lei YL; Moon JJ STING agonist-loaded mesoporous manganese-silica nanoparticles for vaccine applications. J. Controlled Release 2023, 357, 84–93.

(41). Qiao Y; Wotring JW; Zheng Y; Zhang CJ; Zhang Y; Jiang X; Pretto CD; Eyunni S; Parolia A; He T; Cheng C; Cao X; Wang R; Su F; Ellison SJ; Wang Y; Qin J; Yan H; Zhou Q; Ma L; Sexton JZ; Chinnaiyan AM Proxalutamide reduces SARS-CoV-2 infection and associated inflammatory response. Proc. Natl. Acad. Sci. U.S.A 2023, 120 (30), No. e2221809120.

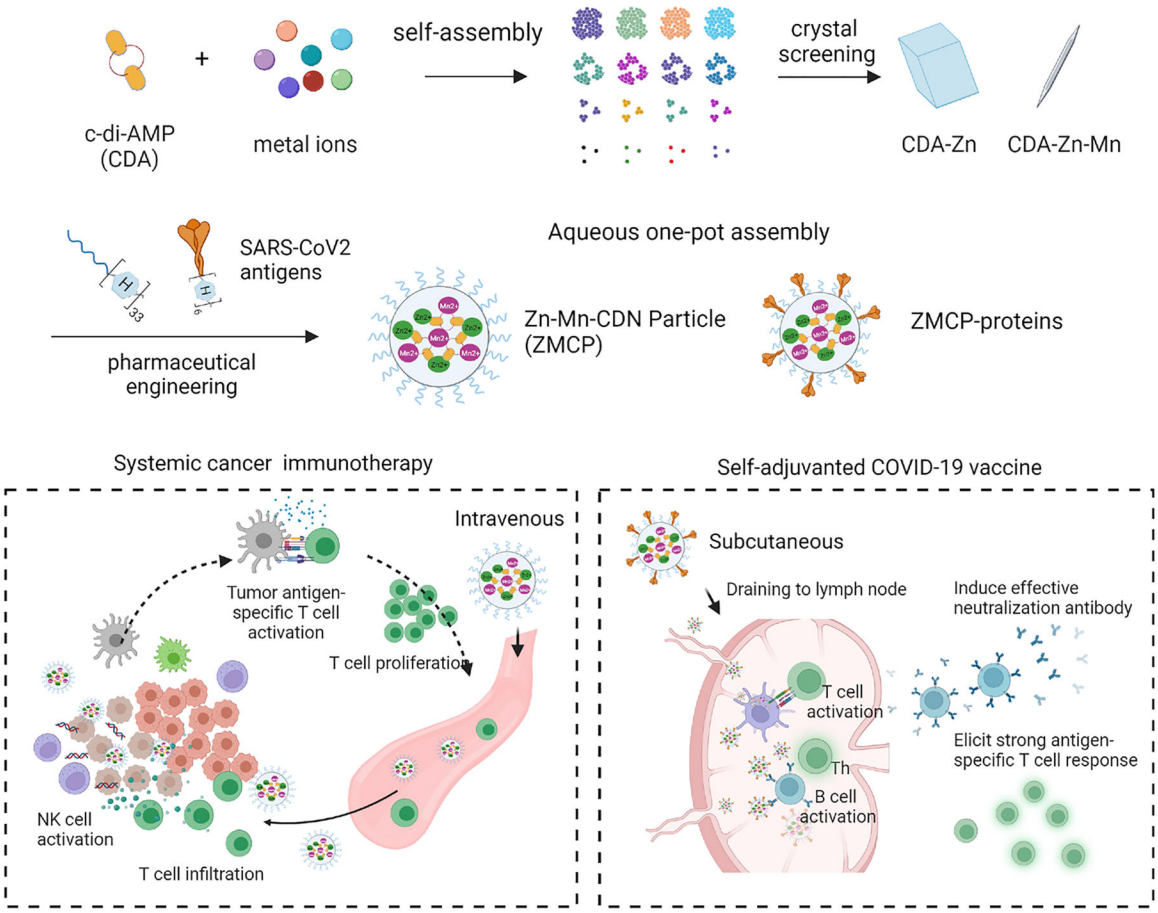

Scheme 1. Aqueous One-Pot Assembly of Cyclic Dinucleotides Coordination Nanoparticle As a STING-Activating Platform for Cancer Immunotherapy and Vaccination against COVID-19[a]

[a](A) Identification of unique macro-scale crystal structures of cyclic di-AMP (CDA)–Zn and CDA–Zn–Mn from screening of aqueous coordination interactions between CDA and metal ions. Further pharmaceutical engineering led to the development of a functional nanoparticle platform, termed Zinc–Mn–CDN Particle (ZMCP). (B) ZMCP enables systemic delivery of CDA for cancer immunotherapy and elicits robust anti-tumor efficacy. (C) ZMCP platform serves as a self-adjuvanted vaccine and ZMCP carrying SARS-CoV-2 antigens elicits strong anti-viral cellular and humoral immune responses. BioRender.com was used to create the scheme.

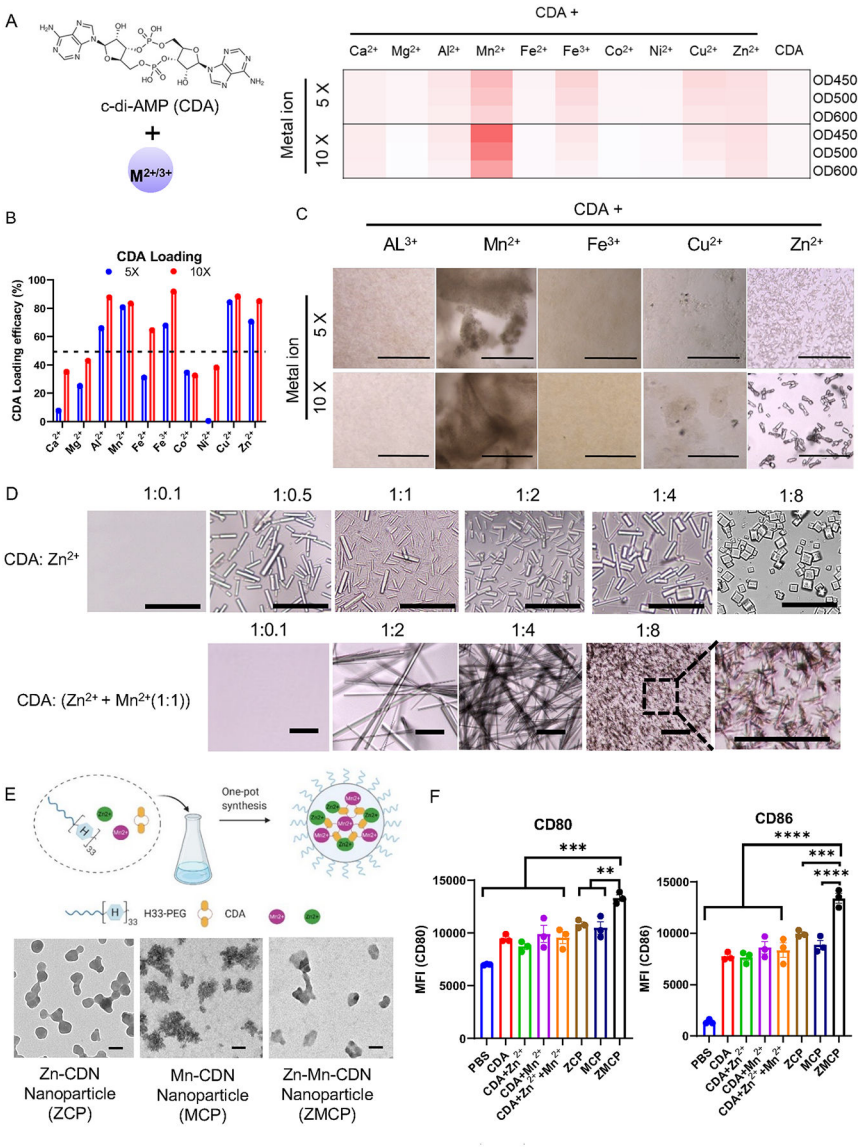

Figure 1.

Development of aqueous one-pot-assembled cyclic dinucleotide (CDN) nanomedicine based on the coordination of CDN with metal ions. (A–D) Screening CDA–metal ion coordination polymorphs. $ZnCl_2$, $MgCl_2$, $MnCl_2$, $CaCl_2$, $Al_2(SO_4)_3$, $CuCl_2$, $FeCl_2$, $FeCl_3$, $NiCl_2$, and $CoCl_2$ solutions in water were added to CDA in 5 or 10 equivalents (n/n), followed by absorbance measurement at OD450 nm, OD500 nm, and OD600 nm (A). The loading efficacy of CDN in the coordination structure (B). Microscopy images of the CDN–metal coordination structures (C). Scale bar: 200 μm. (D) Titrating the ratio of CDA/Zn^{2+} (1:0.1 to 1:8) revealed ratio-dependent change of the crystal geometry, and doping Mn^{2+} into Zn^{2+}/CDA induced needle-like crystals. Scale bar = 200 μm. (E,F) Aqueous one-pot assembly of CDN coordination nanoparticle. (E) CDA, H33-PEG20k, Zn^{2+}, or/and Mn^{2+} were mixed in a one-pot synthesis. The resulting coordination nanoparticles, ZCP, ZMCP, and MCP, were visualized by TEM. Scale bar = 50 nm. (F) BMDCs were treated with

ZMCP, ZCP, MCP, CDA+Mn^{2+}+Zn^{2+}, CDA, or other controls, followed by flow cytometry analysis for the expression of CD80 and CD86. Data represent mean ± SEM, from a representative experiment of two independent experiments with $n = 3$ biological independent samples. *$P < 0.05$, **$P < 0.01$, ***$P < 0.001$, ****$P < 0.0001$, analyzed by one-way ANOVA (F) with Bonferroni's multiple comparisons test.

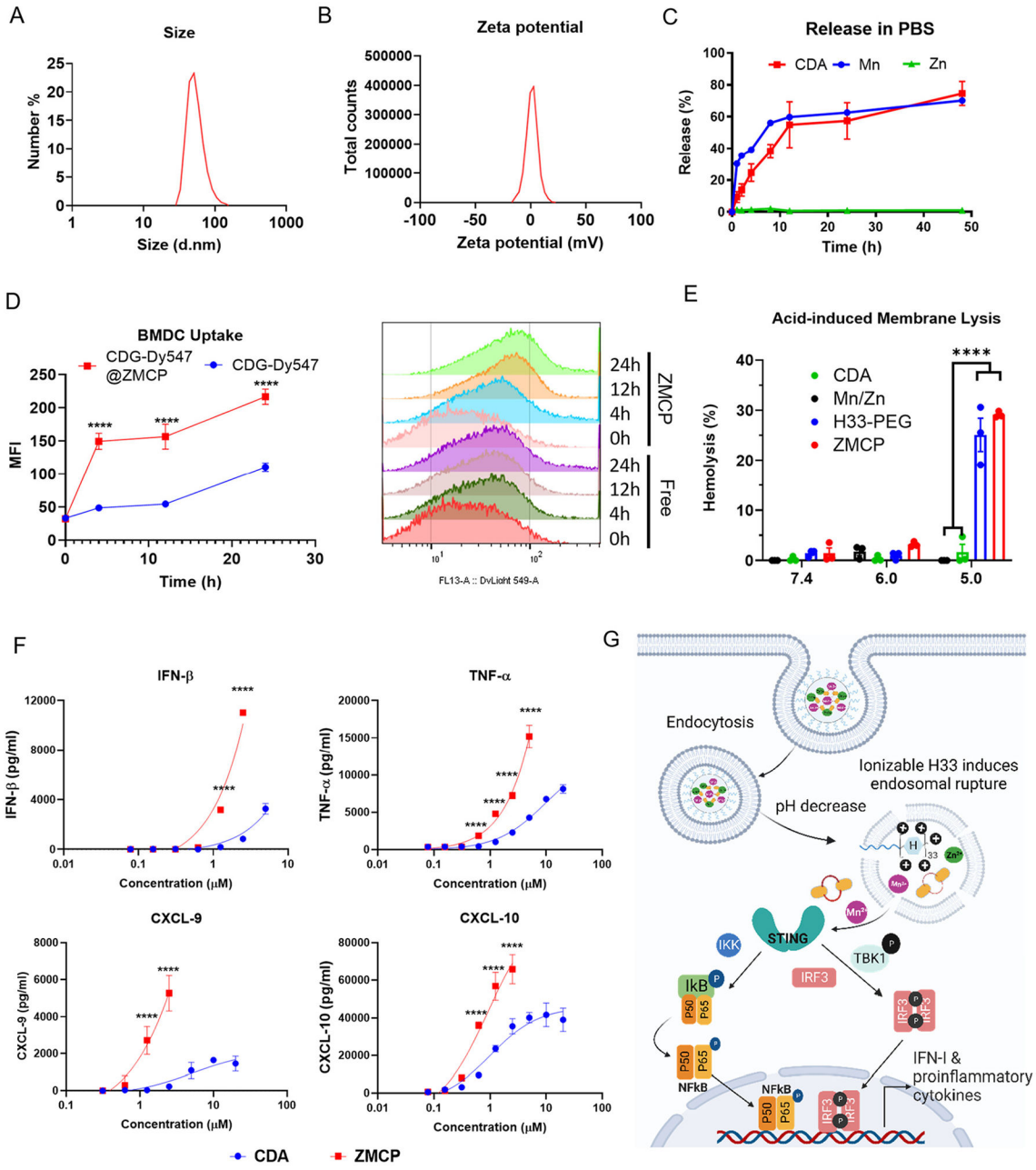

Figure 2.

ZMCP promotes cellular uptake, endosomal escape, and STING activation. (A,B) Hydrodynamic size (A) and zeta potential (B) of ZMCP. (C) Release kinetics of CDA, Mn, and Zn from ZMCP in PBS. (D) Cellular uptake of free CDG-Dy547 or CDG-Dy547@ZMCP by BMDCs over time was analyzed by flow cytometry. (E) As a surrogate marker for endosomal escape, hemolysis of murine red blood cells with ZMCP or soluble controls was measured at pH 7.4, 6, and 5. (F) BMDCs were incubated with ZMCP or CDA for 24 h, followed by ELISA-based measurement of IFN-β, TNF-α, CXCL-9, and CXCL-10 in the media. (G) Schematic mechanism of ZMCP-induced cellular uptake, endosomal escape, and STING activation. Data represent mean ± SEM, from a

representative experiment of two independent experiments with $n = 3$ biological independent samples. $*P < 0.05$, $**P < 0.01$, $***P < 0.001$, $****P < 0.0001$, analyzed by two-way ANOVA (D, E, F) with Bonferroni's multiple comparisons test. BioRender.com was used to create G.

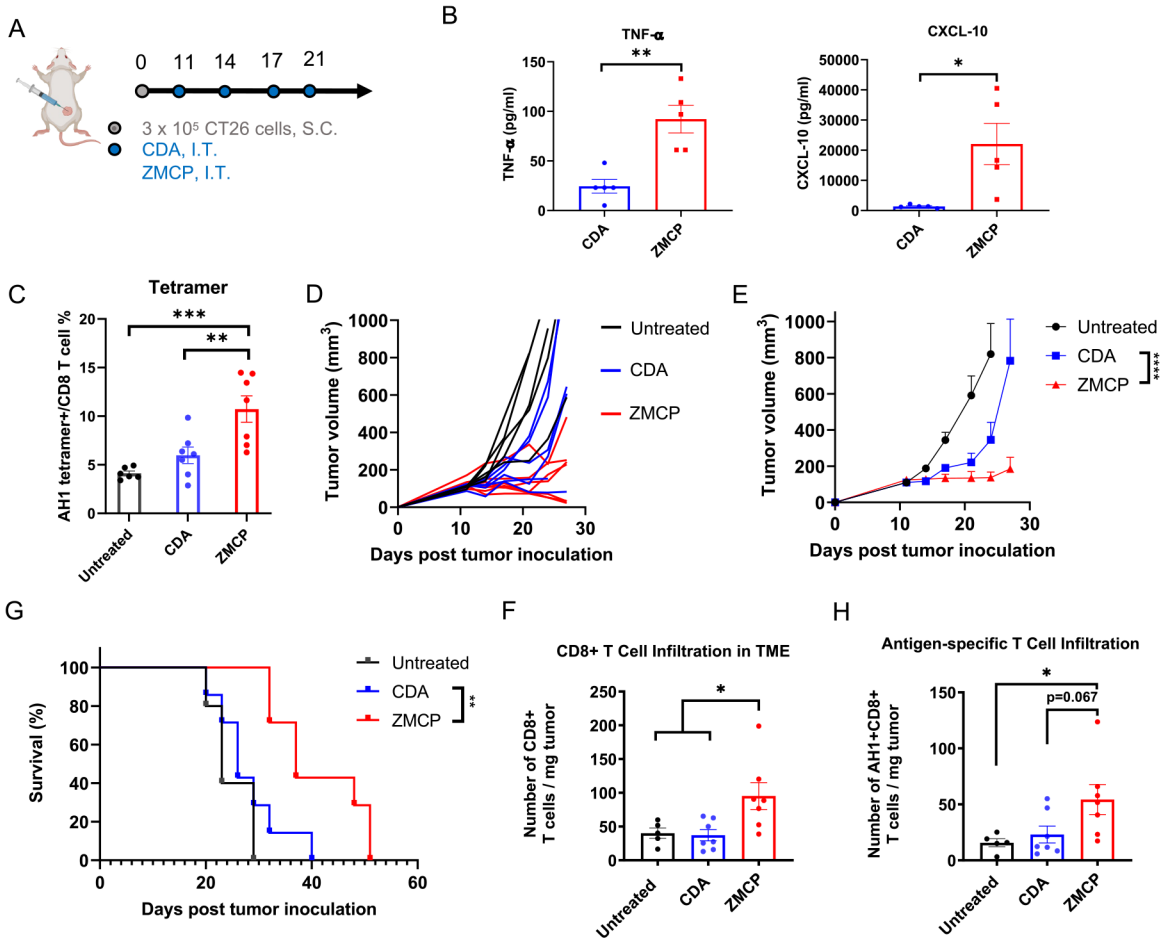

Figure 3.

Intratumoral injection of ZMCP induces antitumor immune responses and inhibits established tumors. (A) BALB/c mice were inoculated at S.C. flank with 3×10^5 CT26 tumor cells. CDA or ZMCP containing 5 μg CDA were injected I.T. on days 11, 14, 17, and 21. (B) Serum cytokines/chemokines were measured by ELISA at 6 h post the second dose. (C) AH1 antigen-specific CD8+ T cell response was analyzed among PBMCs by flow cytometry on day 18. (D–F) ZMCP inhibited tumor growth (D,E) and prolonged animal survival (F). (G) Tumor-infiltrating total CD8+ T cells and (H) AH1 antigen-specific CD8+ T cells were analyzed in the tumor microenvironment by flow cytometry on day 27. Data represent mean ± SEM, from a representative experiment of two independent experiments with $n = 5–8$. *$P < 0.05$, **$P < 0.01$, ***$P < 0.001$, ****$P < 0.0001$, analyzed by two-tailed Student's t test (B), one-way ANOVA (C, G, H), or two-way ANOVA with Bonferroni's multiple comparisons test or log-rank (Mantel-Cox) test (F).

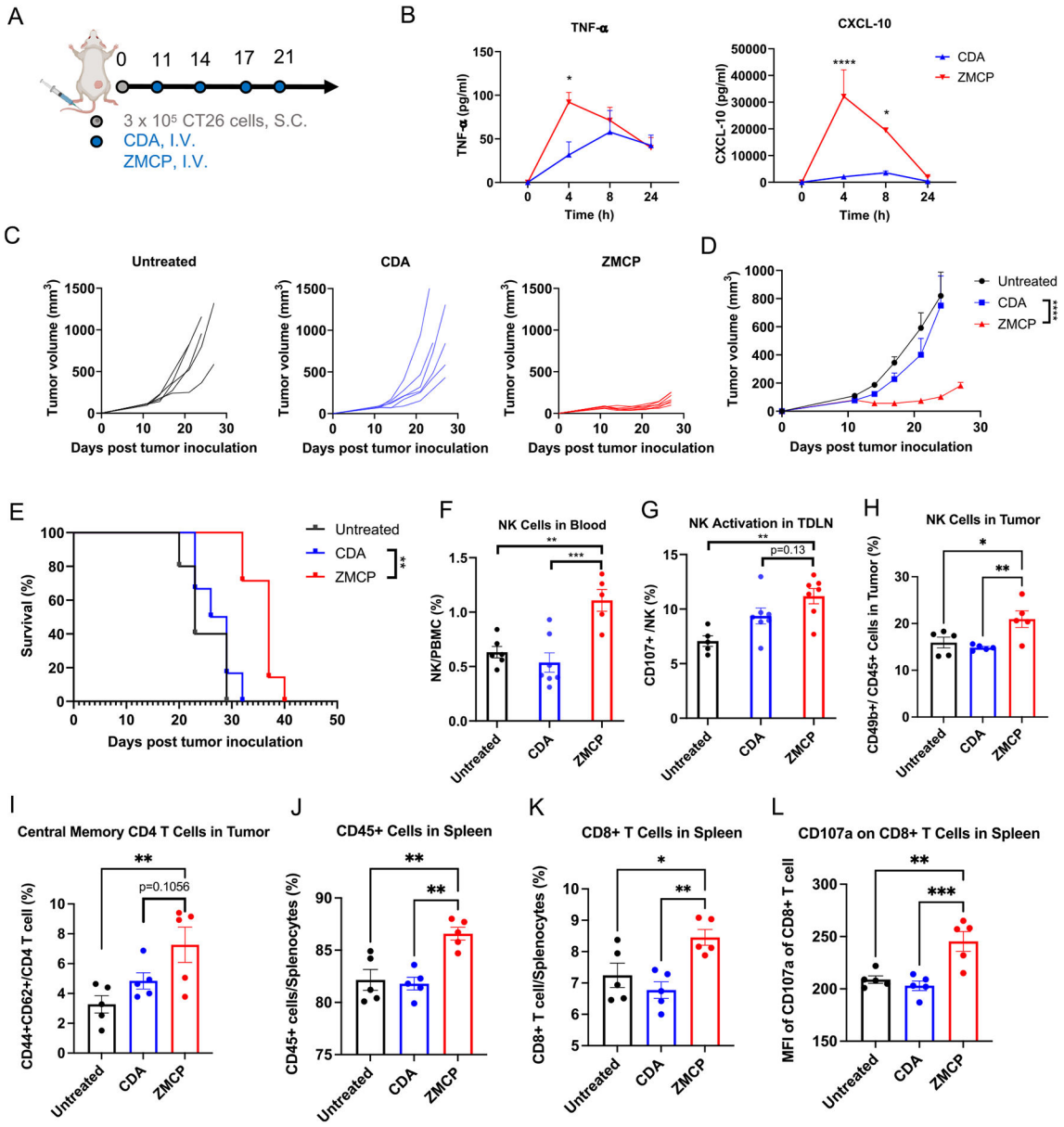

Figure 4.

Intravenous injection of ZMCP effectively induces an antitumor immune response and inhibits growth of established CT26 tumors. (A–G) BALB/c mice were inoculated at the S.C. flank with 3×10^5 CT26 tumor cells. CDA or ZMCP containing 20 μg of CDA were injected I.V. on days 11, 14, 17, and 21 (A). Serum cytokines were measured by ELISA at 0, 4, 8, and 24 h post the second dose (B). Tumor growth (C–D) and animal survival (E) were monitored over time. (F–L) Mice were analyzed on day 27 by flow cytometry for immune cell profiles in PBMCs (F), tumor microenvironment (G–I) and spleen (J–L). Data represent mean ± SEM, from a representative experiment of two independent experiments with n = 5–8. *$P < 0.05$, **$P < 0.01$, ***$P < 0.001$, ****$P < 0.0001$, analyzed by one-way ANOVA (F–L) or two-way ANOVA (B, D) with Bonferroni's multiple comparisons test or log-rank (Mantel-Cox) test (E).

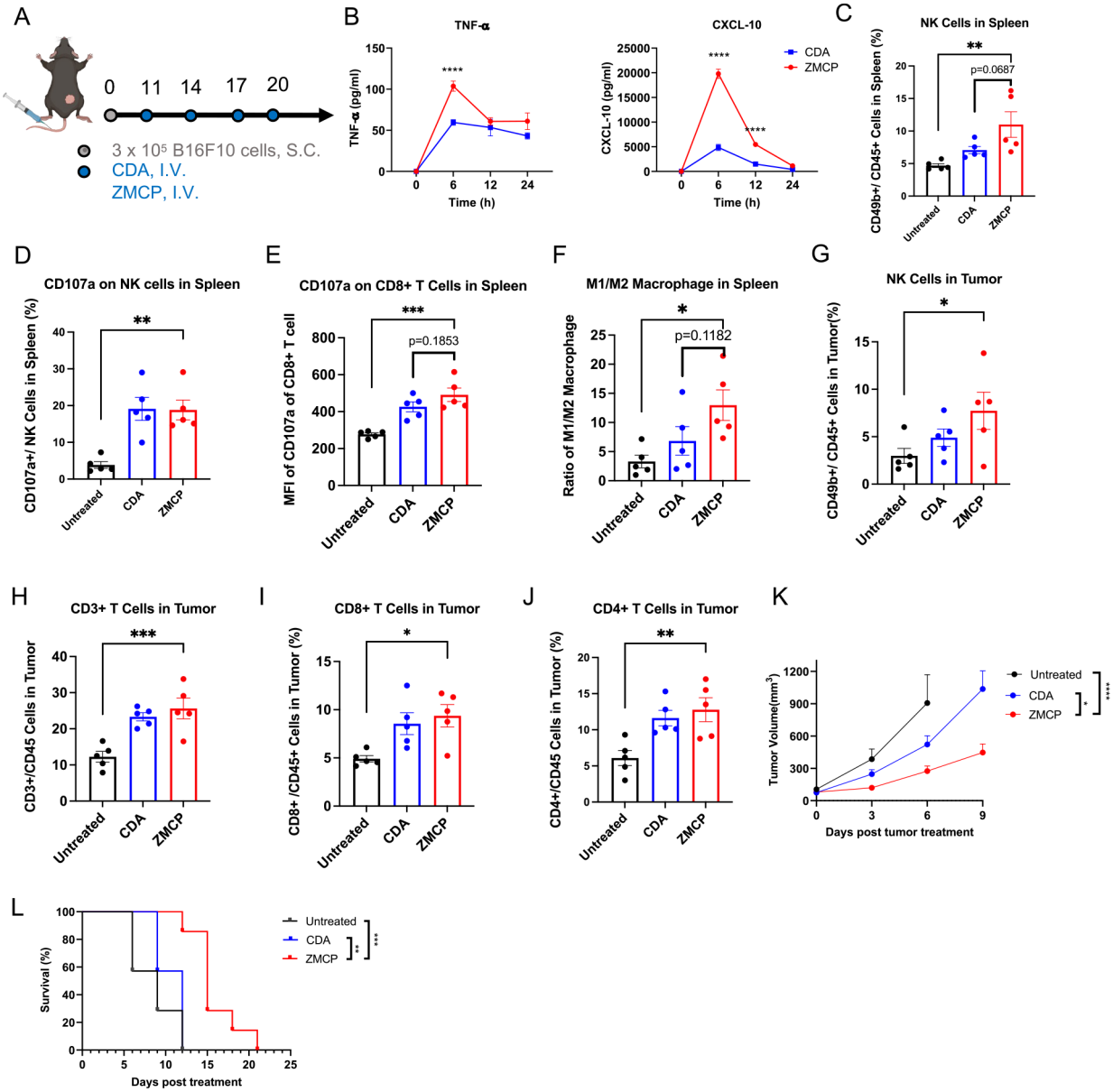

Figure 5.

Intravenous injection of ZMCP effectively induces an antitumor immune response and inhibits tumor growth in an established B16F10 melanoma model. (A) C57BL/6 mice were inoculated at the S.C. flank with 3×10^5 B16F10 tumor cells. CDA or ZMCP containing 20 μg of CDA were injected I.V. on days 11, 14, 17, and 20. (B) Serum cytokines were measured by ELISA at 0, 4, 8, and 24 h post the second dose. (C–J) Mice were analyzed on day 26 by flow cytometry for immune cell profiles in spleens (C–F) and the tumor microenvironment (G–J). (K,L) Tumor growth (K) and animal survival (L) post-treatment were monitored over time. Data represent mean ± SEM, from a representative experiment of two independent experiments with $n = 5–8$. *$P < 0.05$, **$P < 0.01$, ***$P < 0.001$, ****$P < 0.0001$, analyzed by one-way ANOVA (C–J) or two-way ANOVA (B, K) with Bonferroni's multiple comparisons test or log-rank (Mantel-Cox) test (L).

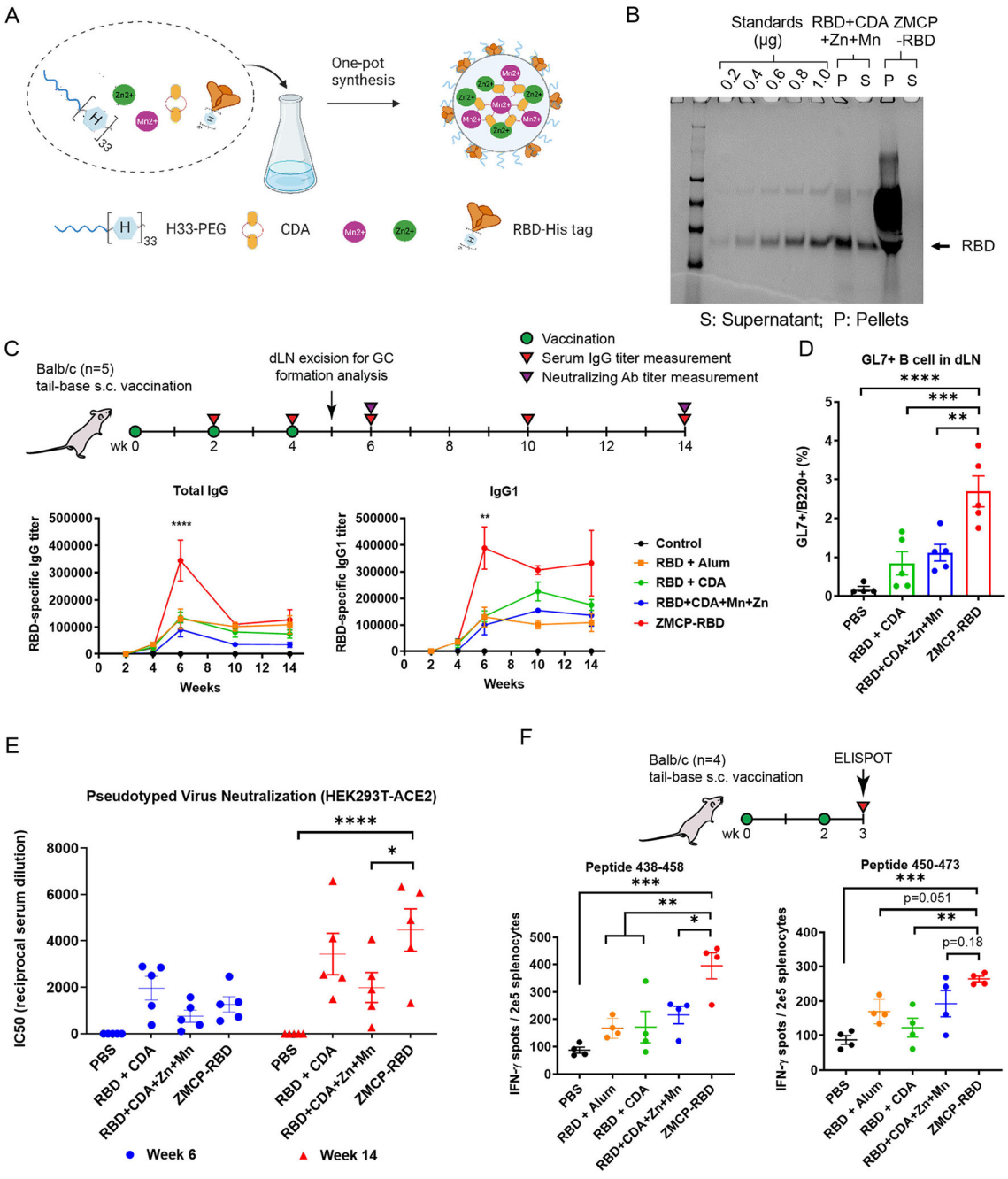

Figure 6.

Delivery of the SARS-CoV2 spike protein receptor binding domain (RBD) by ZMCP as a self-adjuvanted COVID-19 vaccine against virus infection. (A,B) One-pot formulation of ZMCP-RBD. CDA, H33-PEG20k, Zn^{2+}+Mn^{2+}, and RBD-H6 were mixed in a one-pot synthesis (A). Encapsulation of the RBD in nanoparticles was measured by SDS-PAGE (B). (C–E) Balb/c mice were vaccinated three times at the tail base with a two-week interval. Two weeks after each vaccination or 4 and 8 weeks after the last vaccination, sera were analyzed for anti-RBD antibody titer measurement by ELISA (C) and neutralizing

activity using a spike pseudotyped virus (HEK293T-ACE2) (E). Draining LNs (dLNs) were harvested 1 week after the third vaccination for germinal center formation analysis (D). (F) C57BL mice were vaccinated twice at the tail base with a two-week interval. Spleens were harvested 1 week after the last vaccination for ELISPOT assay with $RBD_{438–458}$ and $RBD_{450–473}$. Data represent mean ± SEM, from a representative experiment of two independent experiments with $n = 4–5$. $^{*}P < 0.05$, $^{**}P < 0.01$, $^{***}P < 0.001$, $^{****}P < 0.0001$, analyzed by one-way ANOVA (D, F) or two-way ANOVA (C, E) with Bonferroni's multiple comparisons test. BioRender.com was used to create A.

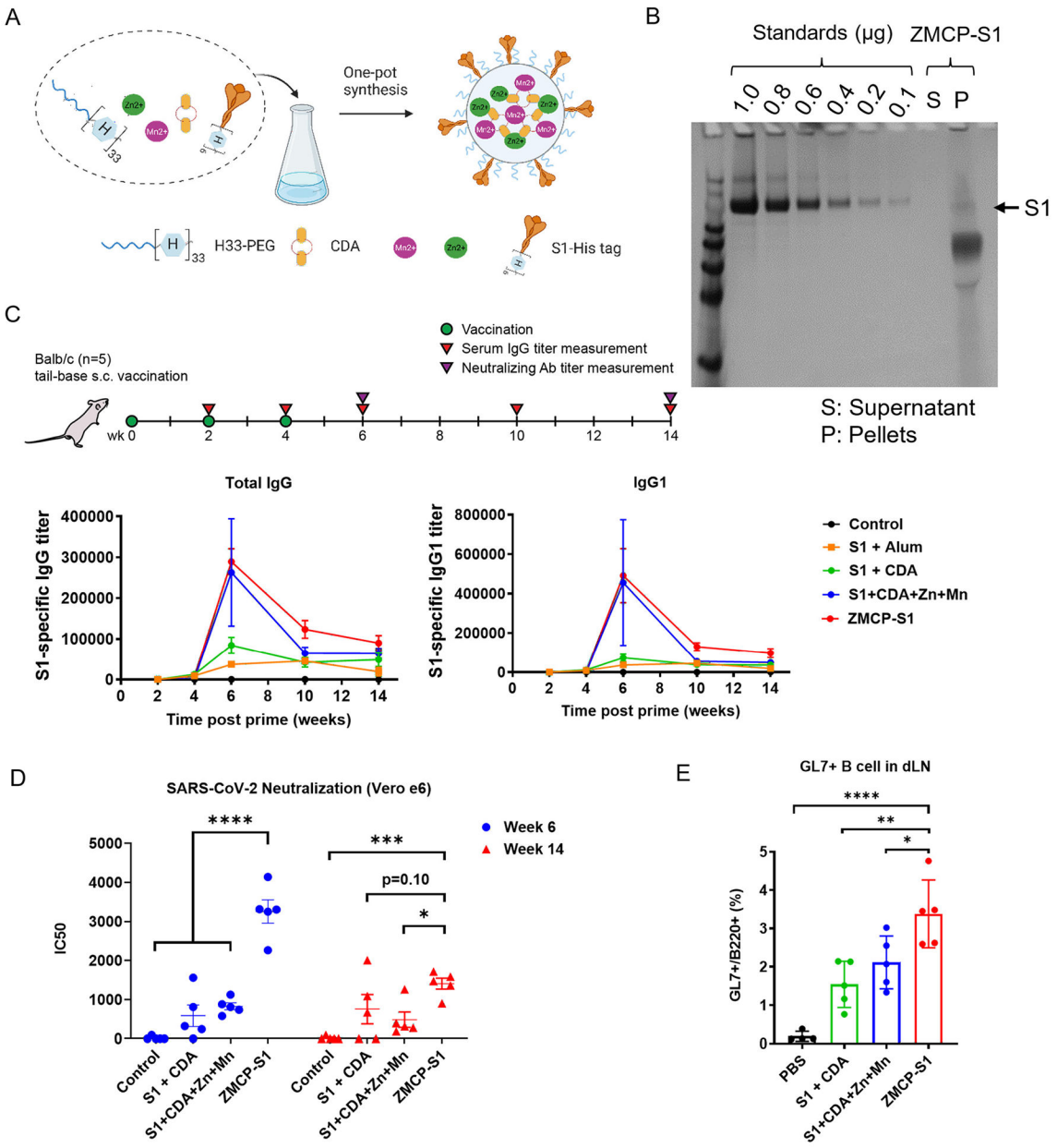

Figure 7.

Delivery of SARS-CoV2 spike protein 1 (S1) by ZMCP as a self-adjuvanted COVID-19 vaccine against virus infectious. (A,B) Schematic for one-pot formulation of ZMCP-S1. CDA, H33-PEG20k, Zn^{2+}, Mn^{2+}, and S1–H6 were mixed in a one-pot synthesis (A). ZMCP-S1 and supernatant were separated by centrifugation, and S1 encapsulated in nanoparticles was measured by SDS-PAGE after particle lysis (B). (C–E) ZMCP-S1 induces an effective humoral immune response against SARS-CoV2. Balb/c mice were vaccinated three times at the tail base with a two-week interval. Sera samples were collected at the indicated time points for S1-specific antibody titer measurement (C) and a viral neutralization assay against SARS-CoV-2 infection in the Vero E6 culture assay (D). Draining LNs were harvested 1 week after the third vaccination and analyzed for germinal

centers (E). Data represent mean ± SEM, from a representative experiment from two to three independent experiments with $n = 4–5$. *$P < 0.05$, **$P < 0.01$, ***$P < 0.001$, ****$P < 0.0001$, analyzed by one-way ANOVA (E) or two-way ANOVA (C, D) with Bonferroni's multiple comparisons test. BioRender.com was used to create A.